Bottom-up configuration-interaction emulations of ultracold fermions in entangled optical plaquettes: Building blocks of unconventional superconductivity

Benedikt B. Brandt,* Constantine Yannouleas,† and Uzi Landman‡
School of Physics, Georgia Institute of Technology, Atlanta, Georgia 30332-0430, USA
(Received 9 December 2016; revised manuscript received 30 January 2017; published 17 April 2017)

A microscopic configuration-interaction (CI) methodology is introduced to enable bottom-up Schrödinger-equation emulation of unconventional superconductivity in ultracold optical traps. We illustrate the method by exploring the properties of ^{6}Li atoms in a single square plaquette in the hole-pairing regime and by analyzing the entanglement (symmetry preserving) and disentanglement physics (via symmetry breaking, associated with the separation of charge and spin density waves) of two coupled plaquettes in the same regime. The single-occupancy resonating valence bond states contribute only partially to the exact many-body solutions and the CI results map onto a Hubbard Hamiltonian, but not onto the double-occupancy-excluding t-J one. For the double-plaquette case, effects brought about by breaking the symmetry between two weakly interacting plaquettes, either by distorting or by tilting and detuning one of the plaquettes with respect to the other, as well as spectral changes caused by increased coupling between the two plaquettes, are explored.

DOI: 10.1103/PhysRevA.95.043617

I. INTRODUCTION

Rapid experimental advances in the creation of finite systems of ultracold atoms using few optical traps (bottom-up) [1–5] or through the use of extended optical lattices (top-down) [6–9] are promising approaches toward realization of Feynman's vision of a quantum simulator [10], capable of finding solutions to systems that are otherwise numerically and/or analytically intractable. However, apart from a few double-well investigations [11–13], to date model-independent microscopic studies of multiwell systems providing theoretical insights and guidance to experimental efforts are largely lacking.

Here we introduce a configuration-interaction (CI) Schrödinger-equation methodology [11,13–16] for exploring finite plaquette systems assembled from individual optical traps; for a brief description of the CI method, see Appendix A. These systems are fundamental stepping stones toward bottom-up realization of large-scale checkerboard or square ultracold-atom lattices, which are promising candidates for emulating the physics underlying d-wave high-T_c superconductivity [17–21] in optical lattices [6–9,22–26]. The work described here, demonstrating the feasibility of such exact CI calculations for interatomic contact interactions, can be extended to electronic plaquettes, i.e., to quantum-dot arrays, governed by long-range Coulomb interactions.

The plan of the paper is as follows. In Sec. II we explore first the properties of ultracold fermionic atoms (^{6}Li) confined in a single square plaquette (four sites) in the regime of hole pairing and subsequently analyze the entanglement physics of two coupled plaquettes in the hole-pairing regime. In Sec. III, for the hole-doped coupled plaquettes (eight sites, six atoms), we analyze the wave-function anatomy of the two entangled [11–13] (Schrödinger-cat) almost-degenerate manifolds, comprising (A) the ground state (GS) and first excited (1EX) state and (B) the two higher excited states (2EX and 3EX). The almost-degenerate states have good, but opposite, parities. When symmetry broken (SB), either by superposing ($\pm$) the degenerate pair in each manifold or via offsetting the energies (tilting) of the two plaquettes, the SB states coming from A are characterized by a particle (charge)-density modulation (wave), i.e., a charge-density wave (CDW) portraying the hole-paired, (4,2) or (2,4), components, whereas the SB states originating from B remain in a (3,3) particle distribution (each of the plaquettes having an unpaired hole), but exhibit a spin-polarization density modulation (wave), i.e., a spin-density wave (SDW). For the double-plaquette case, we further explore effects brought about by breaking the symmetry between two weakly coupled plaquettes, either by distorting one of the plaquettes or by tilting and detuning one of the plaquettes with respect to the other. Spectral changes caused by increased tunnel coupling (e.g., by decreased interplaquette distance) between the two plaquettes are also considered.

Noteworthy is our finding that the GS d-wave resonating valence bond (RVB) state contributes only partially to the exact many-body wave function, i.e., double occupancies (also referred to as doublons) need to be included. Indeed, our microscopic results map properly onto a Hubbard Hamiltonian (including extended Hubbard models [27,28] depending upon the range of the experimental parameters), but not onto the double-occupancy-excluding t-J model [17,18,29]. Our conclusions agree with recent [7–9] observations of doublons in two-dimensional (2D) optical lattices.

The rest of the paper comprises a summary (Sec. IV) and three Appendixes, concerning a brief description of the CI method (Appendix A), the mathematical definitions of single-particle densities and two-body and N-body conditional probability distributions (Appendix B), and the specification of the correspondence between spin and RVB functions and CI many-body wave functions (Appendix C).

*benbra@gatech.edu
†Constantine.Yannouleas@physics.gatech.edu
‡Uzi.Landman@physics.gatech.edu

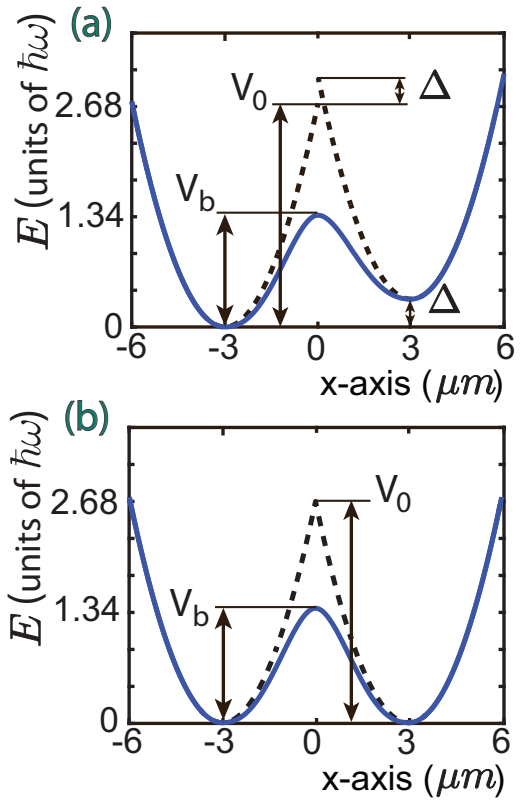

FIG. 1. Illustration of the one-dimensional TCO potential with a smooth neck (solid lines). (a) Case with a tilt $\Delta > 0$. (b) Case without a tilt. Here, and elsewhere, $\hbar\omega$ is the trapping frequency (given in energy units of kHz) of the bare harmonic oscillator (dashed lines) for each site.

II. SINGLE PLAQUETTE

The short-range two-body repulsion in the Hamiltonian is described by a Gaussian function of width σ, i.e., by

$$V(\mathbf{r}_i,\mathbf{r}_j) = \frac{\lambda}{\sigma^2\pi} e^{-(\mathbf{r}_i-\mathbf{r}_j)^2/\sigma^2}, \tag{1}$$

where λ is the strength parameter. Here and throughout the paper $\sigma = \sqrt{2}l_0/10 = 0.1833\ \mu$m, where the oscillator length $l_0^2 = \hbar/(M_{^6\mathrm{Li}}\omega)$, $M_{^6\mathrm{Li}}$ being the ^{6}Li mass and $\hbar\omega = 1$ kHz being the trapping frequency of the plaquette potential wells.[1] This form of interaction provides a good approximation for the atom-atom interactions and avoids the peculiarities of the Dirac δ function in two dimensions [30].

The potential surface of the four-site (or eight-site) plaquette is constructed with the help of the two-center, smooth-neck oscillator Hamiltonian that was previously introduced in Refs. [11,13,15,31]. The smooth-neck interwell barrier V_b can be varied independently and is controlled by the parameter $\epsilon_b = V_b/V_0$, where V_0 is the intersection height of the two bare potential parabolas from neighboring sites, i.e., prior to inserting the smooth-neck potential contribution [11,15,31]. For a graphical illustration of the two-center-oscillator (TCO) double-well potential, including the definitions of V_b and V_0, see Fig. 1. Here and throughout the paper the intersite distance in a single plaquette is $d_w = 6\ \mu$m and $\epsilon_b = 0.5$ (yielding $V_b = 1.34$ kHz), unless noted otherwise. The potential surfaces of the four-site and eight-site plaquettes is constructed by combining such TCO potentials along the x and y directions (see Supplemental Material for details [32]).

The CI single-plaquette low-energy spectrum as a function of the two-body repulsion strength λ is displayed in

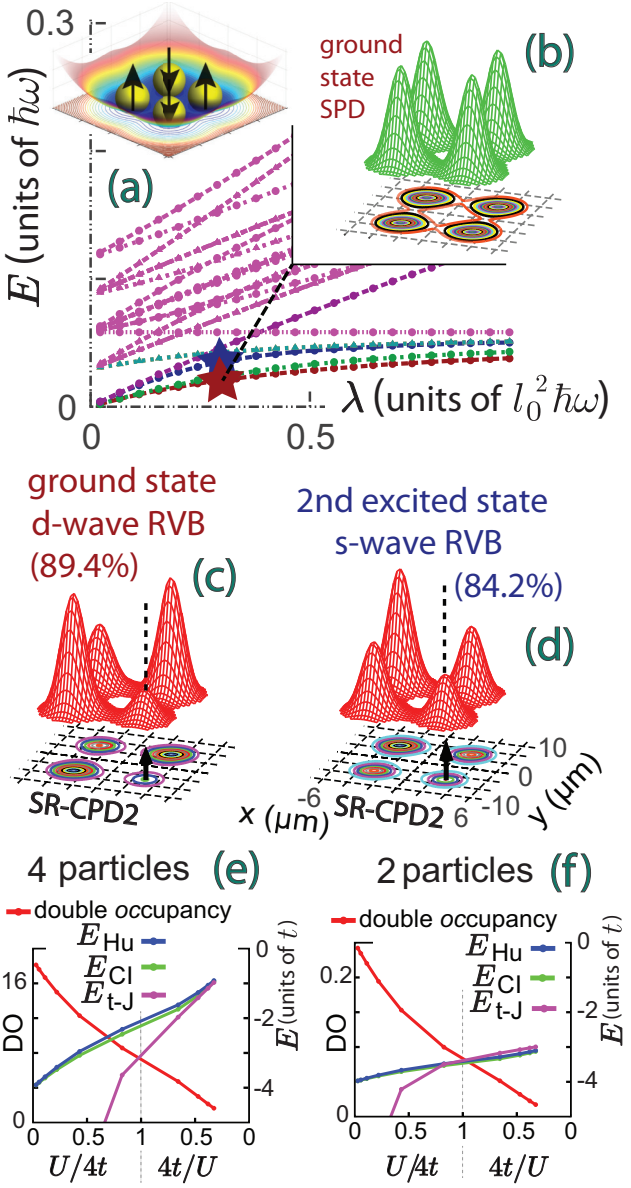

FIG. 2. Configuration-interaction results for ^{6}Li atoms in a four-site plaquette. (a)–(e) Results for $N = 4$ atoms and (f) results for $N = 2$ atoms in a four-site plaquette. (a) Energy spectrum for $V_b = 1.34$ kHz. (b) Ground-state SPD [red star in (a)]. (c) and (d) The SRCPD2s for the GS and 2EX. Up black arrows denote the up-spin at the observation point and red humps the probability for down-spin atoms. Note the double-occupancy hump at the observation point. (e) and (f) Ground-state total energies (E, in units of t) for the CI, Hubbard, and t-J Hamiltonians; the CI double occupancy (DO) is in red. The inset above (a) illustrates the four-site external potential.

[1]The mass of ^{6}Li is taken to be $10\,964.90 m_e$, with m_e the free-electron mass. This gives $l_0 = 1.296\ \mu$m for $\hbar\omega = 1$ kHz.

Fig. 2(a), with the single-particle density (SPD) for the GS (see red star), or for the second excited state (blue star), being shown in Fig. 2(b); for the definition of the SPD in the CI approach, see Appendix B. A total-spin projection $S_z = 0$ has been assumed. The CI wave functions depend on both the atom (continuous) position $\mathbf{r}_i$ and the spin σ_i, $i = 1,2,\ldots,$ variables. However, for plaquettes with sufficiently high interwell barriers, the microscopic structure of a CI state $|\Phi\rangle$ can be mapped onto the usual Hubbard Hilbert space involving the superposition of many primitive basis functions $\Omega_i \equiv |\cdots d \cdots \uparrow \cdots \downarrow \cdots 0 \cdots\rangle$; d here denotes a doubly occupied site, $\uparrow$ and $\downarrow$ denote the site's spin occupancy, and 0 denotes an empty site. The inset in Fig. 2 describes the four-site external potential. The coefficients c_i of the primitives Ω_i in the expansion of $|\Phi\rangle$ can be extracted from the CI wave functions with the help of the spin-resolved conditional probability distributions (SRCPDs) [11,13,33]. Two SRCPDs are used here: one (SRCPD2), expressed as an expectation value over the many-body wave function, describes the space and spin correlation of a particle pair for a given location and spin of one of them (referred to as an observation point) and the other is any other particle of the $N-1$ remaining ones (with a specified spin). The other probability distribution (SRCPDN), given by the modulus square of the many-body function, expresses the spatial probability of finding the Nth particle with a specified spin when one fixes the positions and spins of the other $N-1$ particles (for the mathematical definition of SRCPDs, see Appendix B).

Figures 2(c) and 2(d) display the SRCPD2s of a four-fermion plaquette for the CI states (GS and 2EX) associated with the two stars in Fig. 2(a). The GS SRCPD2 in Fig. 2(c) reveals the presence (89.4%) of a d-wave RVB component and the 2EX SRCPD2 in Fig. 2(d) reveals the presence (84.2%) of an s-wave RVB component (see the analysis in Appendix C); these percentages are derived from the double-occupancy fraction at the fixed-point site [i.e., the hump volume above the arrows in Figs. 2(c) and 2(d)].

The above SRCPD2 analysis points to a deficiency of the t-J model because it excludes [34] double occupancies. We further illustrate the limitations of the t-J model for the full range of the repulsive interaction by plotting for all three approaches (CI, Hubbard, and t-J) the four-fermion and two-fermion total energies E for a single plaquette, as well as the double occupancy, as a function of U/t; see Figs. 2(e) and 2(f), respectively. Evidently, the CI and Hubbard energies, apart from a constant shift, are in very good overall agreement, whereas the t-J values deviate greatly. The exact CI results provide a to-date lacking benchmark for assessments of the validity of the t-J model and its variants [17,18,29,35], as well as the Hubbard-calculated double occupancies.

The hole-pairing gap may be defined in terms of the energies of a four-site plaquette as follows [20]:

$$\Delta_p = 2E_{\rm GS}(N=3) - [E_{\rm GS}(N=4) + E_{\rm GS}(N=2)], \quad (2)$$

where N is the total number of fermions on the plaquette. Configuration-interaction-calculated pairing gaps are shown in Fig. 3 for two interwell distances: $d = 6$ μm [Figs. 3(a) and 3(b)] and $d = 2.5$ μm [Figs. 3(c) and 3(d)]. Figure 3(a) displays Δ_p as a function of the repulsion strength λ and the

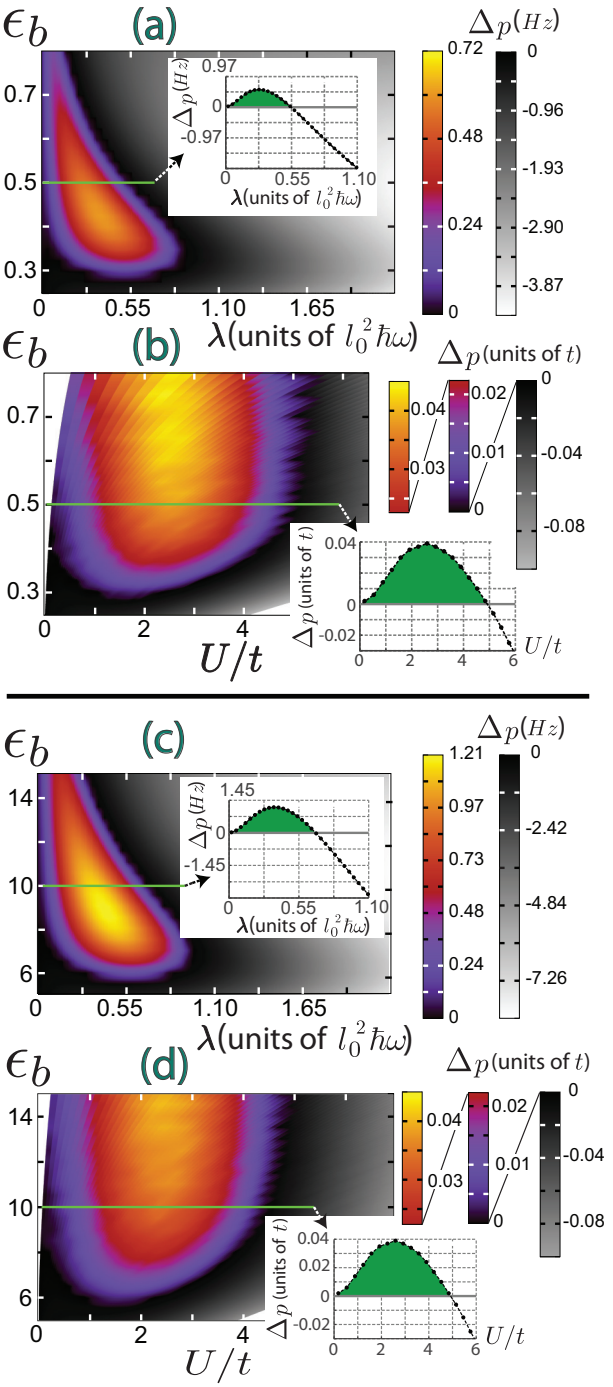

FIG. 3. The CI-calculated contour plot for Δ_p [Eq. (2)] for a single four-well plaquette with variable ϵ_b. For (a) and (b) $d_w = 6$ μm and for (c) and (d) $d_w = 2.5$ μm. Positive values (blue to yellow) indicate pair binding. The horizontal axis in (a) and (c) is the repulsion strength λ and in (b) and (d) it is the extended Hubbard parameter ratio U/t; in (a) and (c) Δ_p is in units of Hz and in (b) and (d) Δ_p is in units of the corresponding hopping parameter t between nearest-neighbor wells. The parameters used in the calculations for the ground states of $N = 4$, $N = 3$, and $N = 2$ fermions are $\hbar\omega = 1$ kHz, $l_0 = 1.296$ μm, $\sigma = 0.184$ μm, and $S = 0$, and $S_z = 0$. In (a) and (b) the barrier height V_b varies from 0.67 kHz ($\epsilon_b = 0.25$) to 2.14 kHz ($\epsilon_b = 0.8$), and in (c) and (d) V_b varies from 2.32 kHz ($\epsilon_b = 5$) to 6.98 kHz ($\epsilon_b = 15$). In (a) and (b) the insets show cuts for intersite barrier $\epsilon_b = 0.5$ and in (c) and (d) the insets show cuts for $\epsilon_b = 10$.

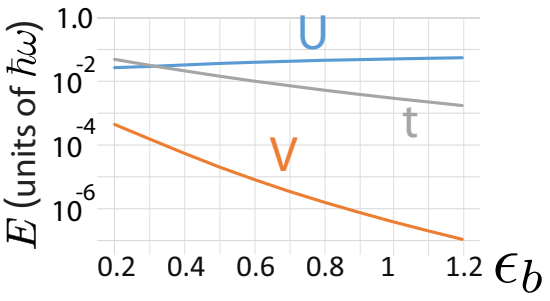

FIG. 4. Evolution of the extended Hubbard parameters U, V, and t as a function of the interwell barrier-height ratio ϵ_b. The distance between the wells is $d_w = 6$ μm, which results in $V_0 = 2.68$ kHz. The remaining trap parameters are $\hbar\omega = 1$ kHz, $l_0 = 1.296$ μm, and $\sigma = 0.184$ μm (note the logarithmic energy scale).

interwell parameter ϵ_b in a single plaquette. The gap maximum ($\sim$0.72 Hz) occurs at ($\lambda \sim 0.30 l_0^2 \hbar\omega, \epsilon_b \sim 0.43$).

To compare with the results of the Hubbard model, Fig. 3(b) displays the same CI results for Δ_p, but with all energies expressed in units of the intersite tunneling parameter t and the interaction strength λ expressed as the ratio U/t, with U being the Hubbard on-site repulsion extracted from the CI calculation. The maximum of Δ_p is now $0.045t$, occurring at ($U/t = 2.6, \epsilon_b \geqslant 0.7$).

When $\epsilon_b > 0.4$ [11,15,31], the maximum value (i.e., $0.045t$) of Δ_p and the range $0 \leqslant U/t < 4.8$, corresponding to $\Delta_p > 0$ (i.e., hole pairing), agree with those found for a single-plaquette pure Hubbard model [20,21,36]. The additional dependence of Δ_p on ϵ_b [see Fig. 3(b)] cannot be described by the standard Hubbard model; it reflects the effect of Hamiltonian terms that are present in the CI calculation, but are absent in the standard Hubbard model, pointing to possible applications of the extended Hubbard Hamiltonian [27,28] in the optical traps assemblage. Particularly relevant here is the off-site repulsion V, which effectively reduces [27] the on-site U. However, V decreases strongly for increasing intersite barrier heights ϵ_b (see Fig. 4), whereas U is highly insensitive. When V becomes sufficiently small relative to U, the standard Hubbard single-plaquette results are recovered [see inset in Fig. 3(b)].

The parameter U in Fig. 4 is the on-site repulsion as determined from the ground-state energy evolution as a function of the interaction strength λ in a single well and V is the intersite repulsive interaction, determined through the matrix element of $V(\mathbf{r}_i, \mathbf{r}_j)$ [see Eq. (1)] taken for the ground-state wave functions, described by Gaussian functions determined through fitting to the CI SPDs. In addition, t is the interwell tunneling parameter, as determined through the energy difference between the two lowest energy states in the y direction (the tunneling split). Note the insensitivity of U vs ϵ_b compared to the strong variation in V. The tunneling parameter t exhibits a reduced sensitivity compared to V. The V term constitutes a perturbation to the pure Hubbard model. When the V term becomes of the order of magnitude of Δ_p, i.e., $0.05t$, the pairing gap vanishes; this happens for values of $\epsilon_b \lesssim 0.3$ for the plaquette considered in this figure.

The role played by the off-site interaction V is further illustrated in Figs. 3(c) and 3(d), where Δ_p is plotted for the case when the intersite distance in the single plaquette is $d_w = 2.5$ nm [compared with $d_w = 6$ nm in Figs. 3(a) and 3(b)]. Clearly much higher values of the intersite potential barriers (i.e., $\epsilon_b > 6$) are required to reach the $\Delta_p > 0$ region.

III. WEAKLY COUPLED TWO-PLAQUETTE MOLECULE

The pairing-gap behavior estimated from a single four-well optical plaquette should be reflected in the properties of a two-plaquette molecule (TPM) when the two plaquettes are weakly coupled (WC). For the single plaquette [Eq. (2) and Fig. 3], Δ_p indicates that the GS of the WC TPM is associated with a (left,right) (4,2) or a (2,4) particle distribution, with the equal-particle arrangement between the (left,right) plaquettes, i.e., (3,3), corresponding to an excited state; $\Delta_p < 0$ indicates reverse energy ordering. The GS and lowest excited-state wave functions of the WC TPM show complex behavior corresponding to entangled two mirror-reflected CDW or SDW symmetry-broken configurations. Experimental probing and quantitative analysis of such entangled states has recently been demonstrated [3], based on inducing particle escape from the optical wells by lowering one side of the trapping potential.

Figure 5 displays CI results for the spectra of $N = 6$ ^{6}Li atoms in two weakly coupled plaquettes separated by $D = 18$ μm. The well separation within the identical plaquettes is $d_w = 6$ μm (Fig. 5, inset), so the intraplaquette barriers are sufficiently high to yield a vanishing off site V (see above). The corresponding low-energy spectrum is plotted versus $-1/\lambda$; the entire spectrum is plotted in Fig. 5(a) and an enlarged view of the spectrum in the interval $-9.5 < 1/\lambda < -7$ is displayed

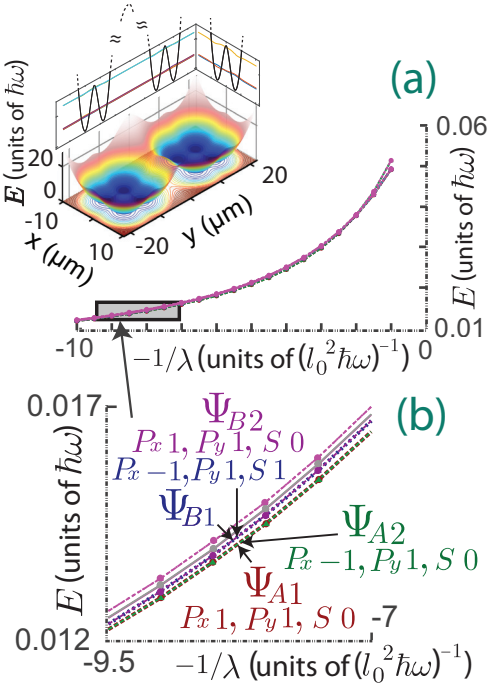

FIG. 5. Configuration-interaction spectra for a double-plaquette WC TPM with interplaquette and intraplaquette distances $D = 18$ μm and $d_w = 6$ μm, respectively. The inset above (a) is an illustration of the external potential for the double plaquette. (a) Spectrum in the extended interval $-10 < -1/\lambda < -1$. (b) Enlarged spectrum in the limited interval $-9.5 < -1/\lambda < -7$.

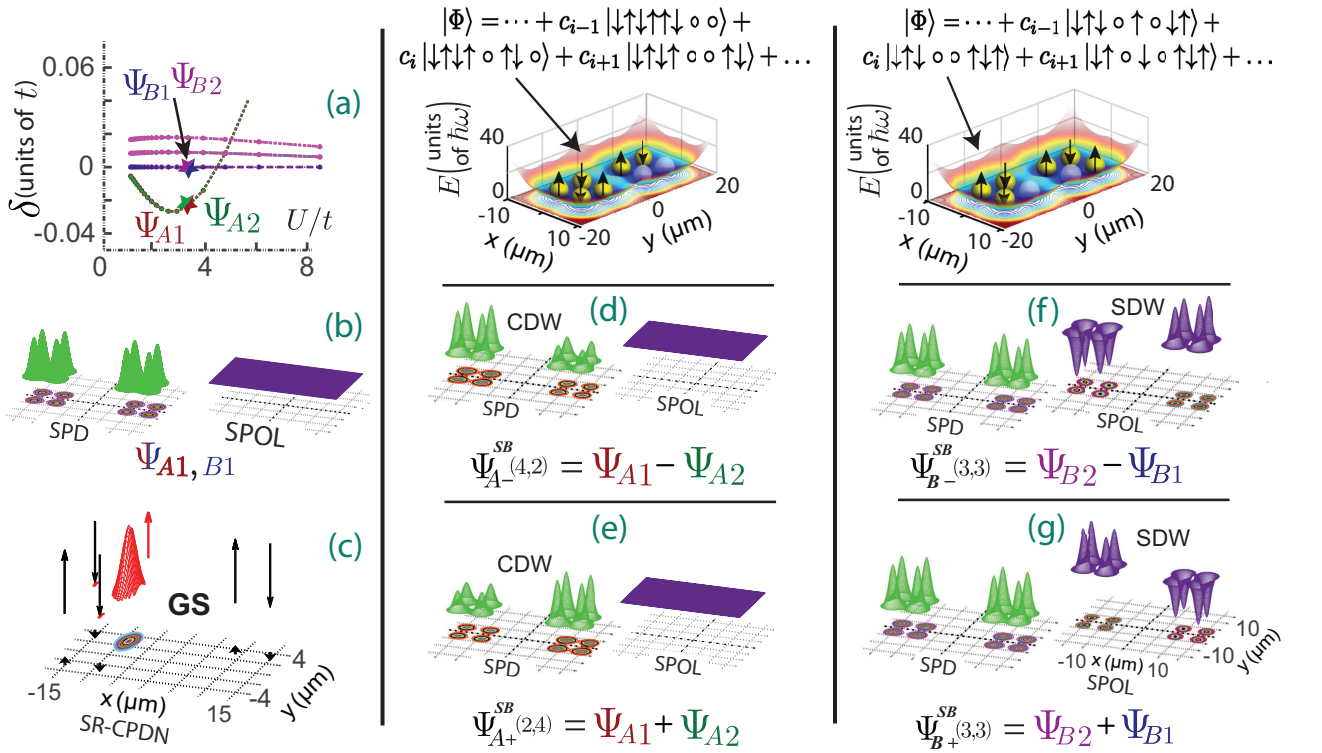

FIG. 6. Configuration-interaction wave functions for a double-plaquette WC TPM with interplaquette and intraplaquette distances $D = 18\ \mu$m and $d_w = 6\ \mu$m, respectively. (a) Subtracted spectrum vs U/t. Here $\delta < 0$ indicates hole pair binding. (b) The SPD and SPOL for the two lowest states $A1$ and $A2$ at the point marked by the stars in (a). (c) The SRCPDN for the GS $A1$ in (a). The observation points (black arrows) form (together with the predicted probability peak (spin-up, red) a (4,2) configuration. (d) and (e) The SPD and SPOL of the symmetry-broken states in the A manifold exhibiting formation of a CDW. (f) and (g) Same as (d) and (e) for the SB states of the B manifold exhibiting formation of a SDW. Top middle inset above (d) and top right inset above (f) give pictorial representations of primitive double-plaquette basis functions corresponding to the (4,2)+(2,4) and (3↑,3↓)+(3↓,3↑) configurations, respectively.

in Fig. 5(b). We focus on the two (lowest) pairs of degenerate states denoted by $(A1, A2)$ and $(B1, B2)$ in Fig. 5(b).

The CI method preserves all the quantum numbers, which are explicitly labeled in Fig. 5, i.e., ± 1 associated with the parities P_x and P_y along the x and y directions and the total spin value $S = 0$ (for $A1$, $A2$, and $B2$) or $S = 1$ (for $B1$). The pairs A and B constitute the four lowest-in-energy states in the whole range $-10 < -1/\lambda < -1$ that we investigated [Fig. 5(b)]. The crossing at $-1/\lambda_c = -2.8$ is reflected in the modified spectrum generated by subtracting the energy $E(B1)$ at each point $-1/\lambda$; see the pocket in Fig. 6(a), where the horizontal axis is expressed now in units of U/t and the crossing occurs at $U/t = 4.8$. For $0 < U/t < 4.8$, the A pair is lower in energy, with the $P_x = 1$, $P_y = 1$, and $S = 0$ state (denoted by $A1$) being the ground state; for $4.8 < U/t$, the B pair is lower in energy, with the $P_x = 1$, $P_y = 1$, and $S = 1$ state (denoted by $B1$) being the ground state.

To investigate the microscopic structure of the states in the A and B pairs, we first display the CI SPDs $[\rho(\mathbf{r},\uparrow) + \rho(\mathbf{r},\downarrow)]$ and spin-polarization densities (SPOLs) $[\rho(\mathbf{r},\uparrow) - \rho(\mathbf{r},\downarrow)]$ for the states $A1$ and $B1$ in Fig. 6(b); see definitions in Appendix B. These CI SPDs and SPOLs are identical for both states, since both parities P_x and P_y, as well as the total spin S, are preserved. In particular, the SPDs exhibit eight humps of equal height, integrating to a total number of $N = 6$ particles. Furthermore, the SPOLs are structureless plane surfaces. The SPDs and SPOLs for the CI states $A2$ and $B2$ exhibit a similar behavior.

Direct insight into the nature of the GS structure is afforded by the SRCPDN shown in Fig. 6(c), where the appearance of a peak in the left plaquette (see red peak), integrating to very close to unit probability for finding an up-spin particle there when fixing the positions and spins of the other five atoms (see black arrows), indicates a dominant (4,2) WC TPM configuration. Little double occupancy is portrayed by small red peaks on diagonal sites (left plaquette).

Although the CI-calculated densities appear uniform across the two plaquettes [see Fig. 6(b)], the microscopic structures of the A and B states are different: They involve different superpositions of many primitive basis functions Ω_i, as exemplified by the $|\Phi\rangle$ superpositions in the insets in Fig. 6. These superpositions contain also primitives with doubly occupied sites (denoted by d earlier, not shown explicitly). For illustrative purposes, the pictorial representations in these panels describe visually one of these primitives associated with the (4,2) (Fig. 6, top middle inset) and the (3,3) (Fig. 6, top right inset) configurations.

As previously mentioned, detailed information can be extracted from the CI wave functions with the help of the SRCPDs [11,13]. However, for $N = 6$ fermions in $M = 8$

sites, calculating the large number of needed CPDs is time consuming. Nevertheless, key features of the hidden anatomy of the entangled states in the A and B pairs can be revealed through the implementation of a forced breaking of their P_x parity symmetry, i.e., by subtracting and adding their member states and constructing the four auxiliary states $A^{\rm SB}_{\mp} = A1 \mp A2$ and $B^{\rm SB}_{\mp} = B1 \mp B2$.

The expectation value of P_x in the $A^{\rm SB}_{\mp}$ and $B^{\rm SB}_{\mp}$ states vanishes; this symmetry breaking results in different characteristics of the above two symmetry-broken states. The SPD for $A^{\rm SB}_{-}$ exhibits a (4,2) particle configuration [Fig. 6(d), left], while the associated SPOL is featureless [Fig. 6(d), right]. The SPD for $A^{\rm SB}_{+}$ corresponds to the mirror-reflected (2,4) configuration [Fig. 6(e), left], with the associated SPOL remaining structureless [Fig. 6(e), right]. The two fermions (or two holes) in the two-particle plaquette are not localized on specific sites. Indeed, after the symmetry breaking, the wave functions are still an entangled superposition of many Ω_i's, thus distributing the particles (or holes) with equal probability over all sites in each plaquette. In a plaquette with two fermions, the volumes under the four density humps integrate to $N = 2$, whereas the volumes under the four density humps in a four-fermion plaquette integrate to $N = 4$. Naturally, the two broken-symmetry states $A^{\rm SB}_{\mp}$ can be characterized as a CDW, because they exhibit a modulation in the SPDs, but none in the spin polarizations.

The SPDs and spin polarizations of the $B^{\rm SB}_{\mp}$ states are displayed in Figs. 6(f) and 6(g). In both cases, the SPDs are symmetric with respect to the left and right plaquettes. Furthermore, the volumes under the humps in each plaquette integrate to $N = 3$, indicating that these states have a (3,3) configuration. However, the left-right asymmetry (due to the broken P_x symmetry) emerges now as an asymmetry in the spin polarization. The three fermions (with total spin $S = 1/2$) in one plaquette have a spin projection $S_z = \pm 1/2$, while the remaining three fermions in the other plaquette have the opposite spin projection $S_z = \mp 1/2$. The $B^{\rm SB}_{\mp}$ broken-symmetry states exhibit SDW characteristics [see the right panels in Figs. 6(f) and 6(g)].

In addition to the above analysis, the (4,2) or (2,4) components of the A states, but not the (3↑,3↓) or (3↓,3↑) components of the B states, can be separated in actual experiments by lifting the left-right degeneracy with the help of two processes: (1) tilting one plaquette with respect to the other [Figs. 7(a)–7(d)] and (2) distorting one of the two plaquettes [Figs. 7(e)–7(h)]. From the CI spectrum depicted in Fig. 7(b), the degeneracy of the states in the A pair is lifted for a tilt $\Delta = 0.1t$, with one of the states becoming the GS at $U/t = 6$ (see the vertical bar). Moreover, the corresponding CI SPD plotted in Fig. 7(d) shows that the tilt induced the symmetry breaking discussed earlier, i.e., a (4.2)

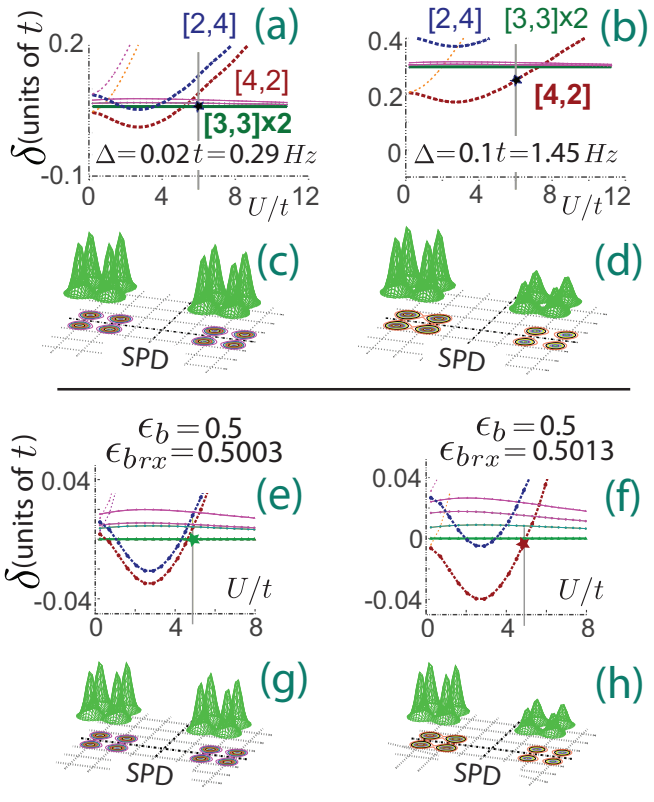

FIG. 7. (a)–(d) Symmetry breaking by applying a tilt Δ or (e)–(h) distorting the internal structure of one of the plaquettes. For the chosen value of U/t in (a) with $\Delta = 0.02t$, no pair binding is observed, as evident from the SPD in (c). However, for a larger tilt $\Delta = 0.1t$, the spectrum in (b) and SPD in (d) indicate GS pair binding, reflecting a (4,2) configuration. Similarly, (e) changing the intraplaquette energy barrier in the right plaquette from $\epsilon_b = 0.5$ to $\epsilon_{brx} = 0.5003$ results in no pair binding [see also SPD in (g)] for the chosen value of U/t, whereas (f) a slightly larger barrier $\epsilon_{brx} = 0.5013$ induces pair-binding as evident from the spectrum in (f) and SPD in (h).

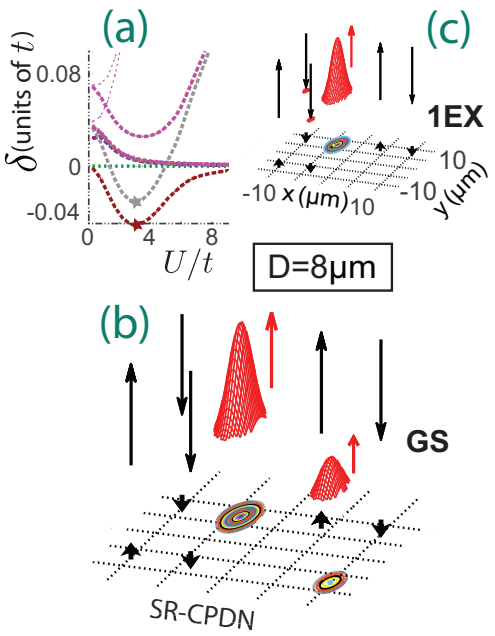

FIG. 8. (a) Configuration-interaction spectrum for a double plaquette with interplaquette and intraplaquette distances $D = 8$ μm and $d_w = 6$ μm, respectively, showing degeneracy splitting between the GS and 1EX [compare with Fig. 6(b), $D = 18$ μm]. (b) and (c) The SRCPDNs corresponding to the GS and 1EX in (a) (see the respective stars) were evaluated for $U/t = 3.5$. The SRCPDN observation points are marked by black arrows with indicated spin directions. The predicted SRCPDNs are denoted in red.

configuration; for smaller tilt results, see Figs. 7(a) and 7(c). Similar symmetry-breaking results, i.e., a spectral energy gap corresponding to the emergence of a (4,2) CDW configuration, are found also for distortions of the plaquette landscape [see Figs. 7(e)–7(h)].

While we focused here on conditions allowing exploration of pure interplaquette entanglement effects, the sensitivity of the energy spectrum and entanglement characteristics to the interplaquette distance (i.e., increasing tunneling between the plaquettes) is illustrated in Figs. 8(a)–8(c), where the spectrum for a double plaquette with $d_w = 6$ μm and $D = 8$ μm is displayed. The spectrum in Fig. 8(a) shows the formation of an energy gap between the two lowest states [compare with Fig. 6(a)]. The SRCPDN in Fig. 8(b), corresponding to the GS at $U/t = 3.5$ (see red star), reflects contributions from both the (4,2) and (4,2) configurations (see the large red peak in the left plaquette and a smaller one in the right plaquette, corresponding to the probabilities of finding spin-up atoms in these locations). On the other hand, the result [Fig. 8(c)] for 1EX [gray star in Fig. 8(a)] portrays the formation of a pure $(4,2) - (2,4)$ configuration [compare to the $(4,2) + (2,4)$ GS of the WC TPM in Fig. 6(c); the small difference between the $+$ and $-$ cases is not visible in the plots].

IV. SUMMARY

In this work we have developed and implemented a configuration-interaction-based computational methodology for obtaining exact solutions to the microscopic many-body quantum Hamiltonian describing ultracold fermionic atoms (here ^{6}Li atoms) moving under the influence of an optically induced multiwell confining potential surface and with short-range interatomic repulsive interactions; we remark here that the same CI methodology can be extended in a straightforward manner to treat interatomic dipolar interactions or confined electrons interacting via long-range Coulomb interactions. A similar type of potential energy surface, made of the assembly of plaquettes, each comprising four sites (potential wells) arranged in a square geometry, has been introduced in early investigations [19,20] of electronic high-temperature superconductivity in cuprate materials, in the context of the two-dimensional Hubbard model often mentioned as a starting point for formulating a theoretical understanding of unconventional superconductivity [37,38].

The Hubbard model was originally derived for the description of the behavior of strongly correlated electrons in solids [39]. However, variants of this model have also been implemented, for over a decade, targeting investigations of strongly interacting ultracold atoms (bosonic or fermionic) in optical lattices, with the interest in such systems originating from remarkable advances in atom cooling and optical trapping techniques, which opened heretofore untapped prospects of preparing, emulating, and measuring the behavior of strongly interacting quantum many-body systems under pristine, defect-free, environments. Analysis of such ultracold-atom emulations of interacting quantum many-body systems revealed on various occasions [28] that many Hubbard models that were simulated with ultracold atoms were found not to have a standard form, meaning that the corresponding Hamiltonians, required for analysis of these results, frequently had to incorporate terms that are not included in the standard Hubbard model and its customary variants. These extra terms may include correlated and occupation-dependent tunneling within the lowest band, as well as correlated tunneling and occupation of higher bands [28].

The above findings connote that progress in developing future ultracold-atom emulations of interacting quantum many-body systems (including quantum magnetism and the origins of unconventional pairing mechanisms) and theoretical methods for the analysis of such emulations (including the development and implementation of effective models such as extended and nonstandard Hubbard Hamiltonians) require benchmark exact calculations (such as the ones introduced in this work), which, owing to their *ab initio* nature, incorporate (with no restriction or approximation) all contributions to the many-body microscopic Hamiltonian. With such computational methodology, one can then proceed to construct, assess, and improve effective models for a reliable analysis of the new forthcoming data. Indeed, in this work we focused on providing benchmark exact quantum-mechanical solutions, aiding and enabling a bottom-up approach aimed at ultracold atoms experiments, and their analysis, starting from a single ultracold-atom plaquette as a building block and progressing in a systematic manner to double plaquettes (with variable interplaquette couplings) and larger, more complex, systems.

Our exact Schrödinger-equation ultracold-fermionic-atom-plaquette simulations demonstrated entangled d- and s-wave RVB states coexisting with partial double occupancies, uncovered hole-pairing phase diagrams, and explored the robustness of the energy spectrum and entanglement of a double-plaquette system (assembled from entangled multipartite plaquettes) through symmetry breaking via interplaquette tilting and distortion and as a function of the strength of interplaquette coupling. These calculations may serve as a foundation for further exact calculations, the development of approximate treatments [40–42], and experiments (including the use of site resolved microscopy enabling direct observation of charge and spin correlations [7–9]) on systems with hierarchically increasing complexity [43–45].

ACKNOWLEDGMENTS

This work was supported by the U.S. Air Force Office of Scientific Research under Grant No. FA9550-15-1-0519. Calculations were carried out at the GATECH Center for Computational Materials Science. We thank R. Schumann for correspondence concerning the analytic Hubbard-model solutions of the four-site plaquette.

APPENDIX A: CONFIGURATION-INTERACTION METHOD

As previously mentioned, we use the method of configuration interaction for determining the solution of the many-body problem specified by the N-fermion general Hamiltonian

$$\mathcal{H}_{\rm MB} = \sum_{i=1}^{N} H(i) + \sum_{i=1}^{N} \sum_{j>i}^{N} V(\mathbf{r}_i, \mathbf{r}_j), \qquad \text{(A1)}$$

where $\mathbf{r}_i$ and $\mathbf{r}_j$ denote the vector positions of the i and j fermions (e.g., ^{6}Li atoms). This Hamiltonian is the sum of a single-particle part $H(i)$, which includes a kinetic energy term and a single-particle external confinement potential (see Fig. 1) that expresses the formation of an interwell barrier between the individual wells and the two-particle interaction $V(\mathbf{r}_i,\mathbf{r}_j)$.

For the case of 2D ultracold atoms, the two-body repulsion is taken as a Gaussian function given by Eq. (1).

In the CI method, one writes the many-body wave function $\Phi_N^{\rm CI}(\mathbf{r}_1,\mathbf{r}_2,\ldots,\mathbf{r}_N)$ as a linear superposition of Slater determinants $\Psi^N(\mathbf{r}_1,\mathbf{r}_2,\ldots,\mathbf{r}_N)$ that span the many-body Hilbert space and are constructed out of the single-particle spin orbitals

$$\chi_j(x,y)=\varphi_j(x,y)\alpha \quad \text{for} \quad 1\leqslant j\leqslant K \tag{A2}$$

and

$$\chi_j(x,y)=\varphi_{j-K}(x,y)\beta \quad \text{for} \quad K<j\leqslant 2K, \tag{A3}$$

where α (β) denotes an up (down) spin, namely,

$$\Phi_{N,q}^{\rm CI}(\mathbf{r}_1,\ldots,\mathbf{r}_N)=\sum_I C_I^q\Psi_I^N(\mathbf{r}_1,\ldots,\mathbf{r}_N), \tag{A4}$$

where

$$\Psi_I^N=\frac{1}{\sqrt{N!}}\begin{vmatrix}\chi_{j_1}(\mathbf{r}_1) & \cdots & \chi_{j_N}(\mathbf{r}_1)\\ \vdots & \ddots & \vdots\\ \chi_{j_1}(\mathbf{r}_N) & \cdots & \chi_{j_N}(\mathbf{r}_N)\end{vmatrix} \tag{A5}$$

and the master index I counts the number of arrangements $\{j_1,j_2,\ldots,j_N\}$ under the restriction that $1\leqslant j_1<j_2<\cdots<j_N\leqslant 2K$. Of course, $q=1,2,\ldots$ counts the excitation spectrum, with $q=1$ corresponding to the ground state.

The many-body Schrödinger equation

$$\mathcal{H}_{\rm MB}\Phi_{N,q}^{\rm CI}=E_{N,q}^{\rm CI}\Phi_{N,q}^{\rm CI} \tag{A6}$$

transforms into a matrix diagonalization problem, which yields the coefficients C_I^q and the eigenenergies $E_{N,q}^{\rm CI}$. Because the resulting matrix is sparse, we implement its numerical diagonalization employing the well known ARPACK solver [46].

The matrix elements $\langle\Psi_I^N|\mathcal{H}|\Psi_J^N\rangle$ between the basis determinants [see Eq. (A5)] are calculated using the Slater rules [16]. Naturally, an important ingredient in this respect is the matrix elements of the two-body interaction

$$\int_{-\infty}^{\infty}\int_{-\infty}^{\infty}d\mathbf{r}_1d\mathbf{r}_2\varphi_i^*(\mathbf{r}_1)\varphi_j^*(\mathbf{r}_2)V(\mathbf{r}_1,\mathbf{r}_2)\varphi_k(\mathbf{r}_1)\varphi_l(\mathbf{r}_2) \tag{A7}$$

in the basis formed out of the single-particle spatial orbitals $\varphi_i(\mathbf{r})$, $i=1,2,\ldots,K$. In our approach, these matrix elements are determined numerically and stored separately.

The Slater determinants Ψ_I^N [see Eq. (A5)] conserve the third projection S_z, but not the square $\hat{\mathbf{S}}^2$ of the total spin. However, because $\hat{\mathbf{S}}^2$ commutes with the many-body Hamiltonian, the CI solutions are automatically eigenstates of $\hat{\mathbf{S}}^2$ with eigenvalues $S(S+1)$. After the diagonalization, these eigenvalues are determined by applying $\hat{\mathbf{S}}^2$ onto $\Phi_{N,q}^{\rm CI}$ and using the relation

$$\hat{\mathbf{S}}^2\Psi_I^N=\left[(N_\alpha-N_\beta)^2/4+N/2+\sum_{i<j}\varpi_{ij}\right]\Psi_I^N, \tag{A8}$$

where the operator ϖ_{ij} interchanges the spins of fermions i and j provided that their spins are different; N_α and N_β denote the number of spin-up and spin-down fermions, respectively.

When there is no tilt [i.e., $\Delta=0$; see Fig. 1(b)], the xy parity operator associated with reflections about the origin of the axes is defined as

$$\hat{\mathcal{P}}_{xy}\Phi_{N,q}^{\rm CI}(\mathbf{r}_1,\mathbf{r}_2,\ldots,\mathbf{r}_N)=\Phi_{N,q}^{\rm CI}(-\mathbf{r}_1,-\mathbf{r}_2,\ldots,-\mathbf{r}_N) \tag{A9}$$

and has eigenvalues ±1. With the separable in x and y basis that we use, it is easy to calculate the parity eigenvalues for the Slater determinants [Eq. (A5)] that span the many-body Hilbert space. The many-body Hamiltonian used in this paper (without an applied magnetic field) conserves also the partial $\hat{\mathcal{P}}_x$ and $\hat{\mathcal{P}}_y$ parities.

APPENDIX B: SINGLE-PARTICLE DENSITIES AND CONDITIONAL PROBABILITY DISTRIBUTIONS: SPD, SPOL, SRCPD2, AND SRCPDN

Denoting the CI wave function by $|\Phi^{\rm CI}\rangle$, the SPD is defined as

$$n(\mathbf{r})=\langle\Phi^{\rm CI}|\sum_{i=1}^N\delta(\mathbf{r}_i-\mathbf{r})|\Phi^{\rm CI}\rangle. \tag{B1}$$

Furthermore, the single-particle SPOL (denoted below by $\mathcal{S}$) is defined as

$$\mathcal{S}(\mathbf{r})=\langle\Phi^{\rm CI}|\sum_{i=1}^N\delta(\mathbf{r}_i-\mathbf{r})\left(\delta_{\uparrow\sigma_i}-\delta_{\downarrow\sigma_i}\right)|\Phi^{\rm CI}\rangle, \tag{B2}$$

where $\uparrow$ and $\downarrow$ denote the up and down values, respectively, of the σ spin variable. The SPOL is the difference between the up and down spin densities.

We probe the intrinsic structure of the CI eigenstates using the spin-resolved conditional probability distribution $P(\mathbf{r}\sigma,\mathbf{r}_0\sigma_0)$ defined by the expression [15,33]

$$P(\mathbf{r}\sigma,\mathbf{r}_0\sigma_0)=\langle\Phi^{\rm CI}|\sum_{i=1}^N\sum_{j\neq i}^N\delta(\mathbf{r}_i-\mathbf{r})\delta(\mathbf{r}_j-\mathbf{r}_0)\delta_{\sigma\sigma_i}\delta_{\sigma_o\sigma_j}|\Phi^{\rm CI}\rangle, \tag{B3}$$

where δ is the Dirac delta function, N is the total number of particles, i and j are particle indices, and σ_i and σ_j represent the spins of particles i and j. The position of the fixed point is $\mathbf{r}_0$ and the spin of the fixed particle is σ_0; r_0 (together with the associated spin at that location σ_0) is referred to as the observation point. Further, σ is the spin of the particle whose spatial distribution we want to know. Since the spin-resolved conditional probability distribution [in Eq. (B3)] is represented by a two-body operator, we denote it by SRCPD2.

However, we found that sometimes SRCPD2s alone are not sufficient to fully decipher the intrinsic configuration of the emerging quantum states. In such a case, one needs to calculate higher correlation functions. In this paper we use the SRCPDN (N-point correlation function) defined as the modulus square of the full many-body CI wave function, i.e.,

$$\begin{aligned}&P(\mathbf{r}\sigma;\mathbf{r}_1\sigma_1,\mathbf{r}_2\sigma_2,\ldots,\mathbf{r}_{N-1}\sigma_{N-1})\\&\quad=|\Phi^{\rm CI}(\mathbf{r}\sigma;\mathbf{r}_1\sigma_1,\mathbf{r}_2\sigma_2,\ldots,\mathbf{r}_{N-1}\sigma_{N-1})|^2,\end{aligned} \tag{B4}$$

where one fixes the positions and spins of $N-1$ particles and inquiries about the (conditional) probability of finding the Nth particle with spin σ at any position $\mathbf{r}$.

APPENDIX C: SPIN EIGENFUNCTION DETERMINATION

1. The RVB state in a single plaquette

In this section we provide a detailed description of the procedure used to identify the d-wave RVB state in our spin-resolved SRCPD2s. As first described in Ref. [15], one can map SRCPD2s to spin eigenfunctions by analyzing the volumes underneath the SRCPD2s. The versatility of this method has been demonstrated several times [13,15] and detailed explanations of the methodology can be found in [13,15,47]. This procedure was carried out by us to identify the RVB states within our plaquettes. The starting point is the general spin eigenfunction for four spin-1/2 fermions trapped in a single plaquette with quantum numbers $S=0$ and $S_z=0$, which is given as [15]

$$\begin{aligned}\chi_{00} = &\sqrt{\frac{1}{3}}\sin\theta|\uparrow\uparrow\downarrow\downarrow\rangle + \left(\frac{1}{2}\cos\theta - \sqrt{\frac{1}{12}}\sin\theta\right)|\uparrow\downarrow\uparrow\downarrow\rangle \\ &- \left(\frac{1}{2}\cos\theta + \sqrt{\frac{1}{12}}\sin\theta\right)|\uparrow\downarrow\downarrow\uparrow\rangle \\ &- \left(\frac{1}{2}\cos\theta + \sqrt{\frac{1}{12}}\sin\theta\right)|\downarrow\uparrow\uparrow\downarrow\rangle \\ &+ \left(\frac{1}{2}\cos\theta - \sqrt{\frac{1}{12}}\sin\theta\right)|\downarrow\uparrow\downarrow\uparrow\rangle + \sqrt{\frac{1}{3}}\sin\theta|\downarrow\downarrow\uparrow\uparrow\rangle. \end{aligned} \tag{C1}$$

This function is parametrized by the angle θ and yields the quantum numbers $S=0$ and $S_z=0$ for all values of θ. The angle θ is a free parameter that for certain values gives spin functions with specified characteristics (e.g., the orthogonal functions mentioned below) or can be treated as a fitting parameter [see the discussion below Eq. (C5) in connection with θ_{CI}]. Equation (C1) expresses in a compact form the fact that the dimension of the total-spin space for $N=4$, $S=0$, and $S_z=0$ is 2; see the branching diagram in Ref. [48] and Ref. [13]. For example, two orthogonal basis functions can be obtained by setting $\theta=0$ and $\theta=\pi/2$. From the general spin function, one can read off the spin components contributing to a specific SRCPD2. For instance, for a spin-down SRCPD2 with a fixed spin-up fermion on position 1 (counting from left to right in the corresponding kets), the spin components contributing to the conditional probability densities are

$$\sqrt{\frac{1}{3}}\sin\theta|\uparrow\uparrow\downarrow\downarrow\rangle, \tag{C2}$$

$$\left(\frac{1}{2}\cos\theta - \sqrt{\frac{1}{12}}\sin\theta\right)|\uparrow\downarrow\uparrow\downarrow\rangle, \tag{C3}$$

$$\left(\frac{1}{2}\cos\theta + \sqrt{\frac{1}{12}}\sin\theta\right)|\uparrow\downarrow\downarrow\uparrow\rangle. \tag{C4}$$

The volume under the hump in position 2 of such a SRCPD2 is therefore proportional to

$$\begin{aligned}\Pi_{\uparrow\downarrow}(1,2) = &\left(\frac{1}{2}\cos\theta - \sqrt{\frac{1}{12}}\sin\theta\right)^2 \\ &+ \left(\frac{1}{2}\cos\theta + \sqrt{\frac{1}{12}}\sin\theta\right)^2. \end{aligned} \tag{C5}$$

This is referred to as the partial conditional probability $\Pi_{\uparrow\downarrow}(1,2)$ (partial because it corresponds to a part of the full SRCPD2, i.e., one peak for a specific spin configuration). Using a normalized SRCPD2. one can directly equate the volume underneath the hump in position 2 to $\Pi_{\uparrow\downarrow}(1,2)$ and determine the angle θ_{CI}. Due to the involved squares, this procedure is not necessarily unique. The unique solution can be found by comparing another hump (i.e., at position 3) to the corresponding partial conditional probability $\Pi_{\uparrow\downarrow}(1,3)$.

However, it is important to note that this procedure is only exact as long as (i) the overlap between sites is sufficiently small and (ii) the amount of double occupancy is small. From Figs. 2(c) and 2(d), it is clear that (i) is fulfilled. To ensure that the possible error due to (ii) is as small as possible, we minimize

$$\begin{aligned}\delta = &[\Pi_{\uparrow\downarrow}(1,2) - \mathcal{V}(2)]^2 + [\Pi_{\uparrow\downarrow}(1,3) - \mathcal{V}(3)]^2 \\ &+ [\Pi_{\uparrow\downarrow}(1,4) - \mathcal{V}(4)]^2, \end{aligned} \tag{C6}$$

where $\mathcal{V}(i)$ represents the volume under the SRCPD2 hump at position i.

2. The d-wave RVB determination

For the ground-state SRCPD2 shown in Fig. 2, this procedure yielded an angle $\theta_{\mathrm{CI}} = 2.618\,614\pi$. It is known that the spin function for the d-wave RVB is given as [26]

$$\begin{aligned}\chi_{d\ \mathrm{RVB}} = &\frac{1}{2\sqrt{3}}|\uparrow\uparrow\downarrow\downarrow\rangle - \frac{1}{\sqrt{3}}|\uparrow\downarrow\uparrow\downarrow\rangle + \frac{1}{2\sqrt{3}}|\uparrow\downarrow\downarrow\uparrow\rangle \\ &+ \frac{1}{2\sqrt{3}}|\downarrow\uparrow\uparrow\downarrow\rangle - \frac{1}{\sqrt{3}}|\downarrow\uparrow\downarrow\uparrow\rangle + \frac{1}{2\sqrt{3}}|\downarrow\downarrow\uparrow\uparrow\rangle, \end{aligned} \tag{C7}$$

which corresponds to an angle of $\theta_{d\ \mathrm{RVB}} = \frac{5\pi}{6}$. We can therefore conclude that our CI results show the presence of a d-wave RVB state with

$$1 - \left|\frac{\theta_{\mathrm{CI}} - \theta_{d\ \mathrm{RVB}}}{\theta_{d\ \mathrm{RVB}}}\right| = 99.98\% \tag{C8}$$

fidelity. However, while the CI result shows the presence of a RVB with high fidelity, the SRCPD2 also undoubtedly shows the presence of double occupancy. The volume of the hump at position 1 amounts to 10.39%. This might seem at first contradictory, but is in fact the correct solution for an interaction strength of $U/t = 2.461$. To show this we calculated the ground-state solution of the Hubbard model

$$H = -t\sum_{\langle i,j\rangle,\sigma}(c^\dagger_{i,\sigma}c_{j,\sigma} + c^\dagger_{j,\sigma}c_{i,\sigma}) + U\sum_{i=1}^{N} n_{i\uparrow}n_{i\downarrow}, \tag{C9}$$

which is given as

$$\begin{aligned}\psi_{\mathrm{GS}} &= 0.455(|\uparrow,\downarrow,\uparrow,\downarrow\rangle + |\uparrow,\downarrow,\uparrow,\downarrow\rangle) + 0.228(-|\uparrow,\uparrow,\downarrow,\downarrow\rangle - |\uparrow,\downarrow,\downarrow,\uparrow\rangle - |\downarrow,\uparrow,\uparrow,\downarrow\rangle - |\downarrow,\downarrow,\uparrow,\uparrow\rangle)\\ &+ 0.149(|\circ,\downarrow,\uparrow,\uparrow\downarrow\rangle - |\circ,\uparrow,\downarrow,\uparrow\downarrow\rangle) + 0.149(|\uparrow,\downarrow,\circ,\uparrow\downarrow\rangle - |\downarrow,\uparrow,\circ,\downarrow\uparrow\rangle) + 0.149(|\downarrow,\circ,\uparrow\downarrow,\uparrow\rangle - |\uparrow,\circ,\uparrow\downarrow,\downarrow\rangle)\\ &+ 0.149(|\uparrow,\downarrow,\uparrow\downarrow,\circ\rangle - |\downarrow,\uparrow,\uparrow\downarrow,\circ\rangle) + 0.149(|\downarrow,\uparrow\downarrow,\circ,\uparrow\rangle - |\uparrow,\uparrow\downarrow,\circ,\downarrow\rangle) + 0.149(|\circ,\uparrow\downarrow,\uparrow,\downarrow\rangle - |\circ,\uparrow\downarrow,\downarrow,\uparrow\rangle)\\ &+ 0.149(|\uparrow\downarrow,\circ,\downarrow,\uparrow\rangle - |\uparrow\downarrow,\circ,\uparrow,\downarrow\rangle) + 0.149(|\uparrow\downarrow,\uparrow,\downarrow,\circ\rangle - |\uparrow\downarrow,\downarrow,\uparrow,\circ\rangle)\\ &+ 0.078(-|\circ,\circ,\uparrow\downarrow,\uparrow\downarrow\rangle + |\circ,\uparrow\downarrow,\uparrow\downarrow,\circ\rangle + |\uparrow\downarrow,\circ,\circ,\uparrow\downarrow\rangle - |\uparrow\downarrow,\uparrow\downarrow,\circ,\circ\rangle)\\ &= 0.79\chi_{d\ \mathrm{RVB}} + 0.38\chi_{\mathrm{DO}} \end{aligned} \tag{C10}$$

The first two lines of Eq. (C10) are the d-wave RVB component and appear with dominant coefficients; however, the wave function clearly contains contributions from doubly occupied states (represented as χ_{DO}). Summing the squared coefficients of the spin primitives that contain doubly occupied sites yields a double occupancy of 10.17% in excellent agreement with the CI result.

3. The s-wave RVB determination

The same analysis can be performed for the s-wave RVB state. The spin function for an s-wave RVB state is given in literature as [24,26]

$$\chi_{s\ \mathrm{RVB}} = \tfrac{1}{2}(|\uparrow\uparrow\downarrow\downarrow\rangle + |\downarrow\downarrow\uparrow\uparrow\rangle - |\downarrow\uparrow\uparrow\downarrow\rangle - |\uparrow\downarrow\downarrow\uparrow\rangle). \tag{C11}$$

This corresponds to an angle of $\theta_{s\ \mathrm{RVB}} = -\frac{2\pi}{3}$. The angle determined from our CI is $\theta_{\mathrm{CI}} = -0.666\,32\pi$, corresponding to a fidelity of

$$1 - \left|\frac{\theta_{\mathrm{CI}} - \theta_{s\ \mathrm{RVB}}}{\theta_{s\ \mathrm{RVB}}}\right| = 99.95\%. \tag{C12}$$

However, just like the ground-state SRCPD2, the SRCPD2 for the second excited state shows a nonzero double occupancy. Therefore, we computed the Hubbard model solution for the second excited state at $U/t = 2.461$:

$$\begin{aligned}\psi_{2\mathrm{EX}} &= 0.361(-|\uparrow,\uparrow,\downarrow,\downarrow\rangle + |\uparrow,\downarrow,\downarrow,\uparrow\rangle + |\downarrow,\uparrow,\uparrow,\downarrow\rangle - |\downarrow,\downarrow,\uparrow,\uparrow\rangle) + 0.185(-|\uparrow\downarrow,\circ,\uparrow\downarrow,\circ\rangle - |\circ,\uparrow\downarrow,\circ,\uparrow\downarrow\rangle)\\ &+ 0.153(|\circ,\downarrow,\uparrow,\uparrow\downarrow\rangle - |\circ,\uparrow,\downarrow,\uparrow\downarrow\rangle) + 0.153(-|\uparrow,\downarrow,\circ,\uparrow\downarrow\rangle + |\downarrow,\uparrow,\circ,\downarrow\uparrow\rangle) + 0.153(|\downarrow,\circ,\uparrow\downarrow,\uparrow\rangle - |\uparrow,\circ,\uparrow\downarrow,\downarrow\rangle)\\ &+ 0.153(-|\uparrow,\downarrow,\uparrow\downarrow,\circ\rangle + |\downarrow,\uparrow,\uparrow\downarrow,\circ\rangle) + 0.153(|\downarrow,\uparrow\downarrow,\circ,\uparrow\rangle - |\uparrow,\uparrow\downarrow,\circ,\downarrow\rangle) + 0.153(-|\circ,\uparrow\downarrow,\uparrow,\downarrow\rangle + |\circ,\uparrow\downarrow,\downarrow,\uparrow\rangle)\\ &+0.153(|\uparrow\downarrow,\circ,\downarrow,\uparrow\rangle - |\uparrow\downarrow,\circ,\uparrow,\downarrow\rangle) + 0.153(-|\uparrow\downarrow,\uparrow,\downarrow,\circ\rangle + |\uparrow\downarrow,\downarrow,\uparrow,\circ\rangle)\\ &+0.093(-|\circ,\circ,\uparrow\downarrow,\uparrow\downarrow\rangle - |\circ,\uparrow\downarrow,\uparrow\downarrow,\circ\rangle - |\uparrow\downarrow,\circ,\circ,\uparrow\downarrow\rangle - |\uparrow\downarrow,\uparrow\downarrow,\circ,\circ\rangle)\\ &= 0.72\chi_{s\ \mathrm{RVB}} + 0.48\chi_{\mathrm{DO}}. \end{aligned} \tag{C13}$$

This eigenfunction predicts a double occupancy on site 1 of 14.52%. The volume of the hump on position 1 indicating double occupancy in our CI amounts to 15.78%, in good agreement with the Hubbard result.

[1] G. Zürn, F. Serwane, T. Lompe, A. N. Wenz, M. G. Ries, J. E. Bohn, and S. Jochim, Fermionization of Two Distinguishable Fermions, Phys. Rev. Lett. **108**, 075303 (2012).

[2] S. Murmann, A. Bergschneider, V. M. Klinkhamer, G. Zürn, T. Lompe, and S. Jochim, Two Fermions in a Double Well: Exploring a Fundamental Building Block of the Hubbard Model, Phys. Rev. Lett. **114**, 080402 (2015).

[3] S. Murmann, F. Deuretzbacher, G. Zürn, J. Bjerlin, S. M. Reimann, L. Santos, T. Lompe, and S. Jochim, Antiferromagnetic Heisenberg Spin Chain of a Few Cold Atoms in a One-Dimensional Trap, Phys. Rev. Lett. **115**, 215301 (2015).

[4] A. M. Kaufman, B. J. Lester, C. M. Reynolds, M. L. Wall, M. Foss-Feig, K. R. A. Hazzard, A. M. Rey, and C. A. Regal, Two-particle quantum interference in tunnel-coupled optical tweezers, Science **345**, 306 (2014).

[5] A. M. Kaufman, B. J. Lester, M. Foss-Feig, M. L. Wall, A. M. Rey, and C. A. Regal, Entangling two transportable neutral atoms via local spin exchange, Nature (London) **527**, 208 (2015).

[6] R. A. Hart, P. M. Duarte, T.-L. Yang, X. Liu, Th. Paiva, E. Khatami, R. T. Scalettar, N. Trivedi, D. A. Huse, and R. G. Hulet, Observation of antiferromagnetic correlations in the Hubbard model with ultracold atoms, Nature (London) **519**, 211 (2015).

[7] M. Boll, T. A. Hilker, G. Salomon, A. Omran, J. Nespolo, L. Pollet, I. Bloch, and C. Gross, Spin- and density-resolved microscopy of antiferromagnetic correlations in Fermi-Hubbard chains, Science **353**, 1257 (2016).

[8] M. F. Parsons, A. Mazurenko, C. S. Chiu, G. Ji, D. Greif, and M. Greiner, Site-resolved measurement of the spin-correlation function in the Fermi-Hubbard model, Science **353**, 1253 (2016).

[9] L. W. Cheuk, M. A. Nichols, K. R. Lawrence, M. Okan, H. Zhang, E. Khatami, N. Trivedi, T. Paiva, M. Rigol, and M. W. Zwierlein, Observation of spatial charge and spin correlations in the 2D Fermi-Hubbard model, Science **353**, 1260 (2016).

[10] R. P. Feynman, Simulating physics with computers, Int. J. Theor. Phys. **21**, 467 (1982).

[11] B. B. Brandt, C. Yannouleas, and U. Landman, Double-well ultracold-fermions computational microscopy: Wave-function anatomy of attractive-pairing and Wigner-molecule entanglement and natural orbitals, Nano Lett. **15**, 7105 (2015).

[12] M. A. García-March, A. Yuste, B. Juliá-Díaz, and A. Polls, Mesoscopic superpositions of Tonks-Girardeau states and the Bose-Fermi mapping, Phys. Rev. A **92**, 033621 (2015).

[13] C. Yannouleas, B. B. Brandt, and U. Landman, Ultracold few fermionic atoms in needle-shaped double wells: Spin chains and resonating spin clusters from microscopic Hamiltonians emulated via antiferromagnetic Heisenberg and t-J models, New J. Phys. **18**, 073018 (2016).

[14] C. Yannouleas and U. Landman, Symmetry breaking and quantum correlations in finite systems: studies of quantum dots and ultracold Bose gases and related nuclear and chemical methods, Rep. Prog. Phys. **70**, 2067 (2007).

[15] Ying Li, C. Yannouleas, and U. Landman, Artificial quantum-dot helium molecules: Electronic spectra, spin structures, and Heisenberg clusters, Phys. Rev. B **80**, 045326 (2009).

[16] A. Szabo and N. S. Ostlund, *Modern Quantum Chemistry* (McGraw-Hill, New York, 1989).

[17] P. W. Anderson, P. A. Lee, M. Randeria, T. M. Rice, N. Trivedi, and F. C. Zhang, The physics behind high-temperature superconducting Cuprates: The "Plain Vanilla" version of RVB, J. Phys.: Condens. Matter **16**, R755 (2004); P. W. Anderson, Who or what is RVB?, Phys. Today **61**, 8 (2008).

[18] M. Ogata and H. Fukuyama, The t-J model for the oxide high-T_c superconductors, Rep. Prog. Phys. **71**, 036501 (2008).

[19] D. J. Scalapino and S. A. Trugman, Local antiferromagnetic correlations and $d_{x^2-y^2}$ pairing, Philos. Mag. B **74**, 607 (1996).

[20] W.-F. Tsai and S. A. Kivelson, Superconductivity in inhomogeneous Hubbard models, Phys. Rev. B **73**, 214510 (2006).

[21] W.-F. Tsai, Inhomogeneous Hubbard models, Ph.D. thesis, University of California, Los Angeles, 2008.

[22] W. Hofstetter, J. I. Cirac, P. Zoller, E. Demler, and M. D. Lukin, High-Temperature Superfluidity of Fermionic Atoms in Optical Lattices, Phys. Rev. Lett. **89**, 220407 (2002).

[23] S. Trebst, U. Schollwöck, M. Troyer, and P. Zoller, d-Wave Resonating Valence Bond States of Fermionic Atoms in Optical Lattices, Phys. Rev. Lett. **96**, 250402 (2006).

[24] A. M. Rey, R. Sensarma, S. Fölling, M. Greiner, E. Demler, and M. D. Lukin, Controlled preparation and detection of d-wave superfluidity in two-dimensional optical superlattices, Europhys. Lett. **87**, 60001 (2009).

[25] B. Paredes and I. Bloch, Minimum instances of topological matter in an optical plaquette, Phys. Rev. A **77**, 023603 (2008).

[26] S. Nascimbène, Y.-A. Chen, M. Atala, M. Aidelsburger, S. Trotzky, B. Paredes, and I. Bloch, Experimental Realization of Plaquette Resonating Valence-Bond States with Ultracold Atoms in Optical Superlattices, Phys. Rev. Lett. **108**, 205301 (2012).

[27] L. M. Falicov and R. A. Harris, Two-electron homopolar molecule: A test for spin-density waves and charge-density waves, J. Chem. Phys. **51**, 3153 (1969).

[28] O. Dutta, M. Gajda, Ph. Hauke, M. Lewenstein, D.-S. Lühmann, B. A. Malomed, T. Sowiński, and J. Zakrzewski, Non-standard Hubbard models in optical lattices: A review, Rep. Prog. Phys. **78**, 066001 (2015).

[29] F. C. Zhang and T. M. Rice, Effective Hamiltonian for the superconducting Cu oxides, Phys. Rev. B **37**, 3759(R) (1988).

[30] R. A. Doganov, S. Klaiman, O. E. Alon, A. I. Streltsov, and L. S. Cederbaum, Two trapped particles interacting by a finite-range two-body potential in two spatial dimensions, Phys. Rev. A **87**, 033631 (2013).

[31] C. Yannouleas and U. Landman, Spontaneous Symmetry Breaking in Single and Molecular Quantum Dots, Phys. Rev. Lett. **82**, 5325 (1999); **85**, 2220(E) (2000).

[32] See Supplemental Material at http://link.aps.org/supplemental/10.1103/PhysRevA.95.043617 for details.

[33] L. O. Baksmaty, C. Yannouleas, and U. Landman, Rapidly rotating boson molecules with long- or short-range repulsion: An exact diagonalization study, Phys. Rev. A **75**, 023620 (2007).

[34] A. Paramekanti, M. Randeria, and N. Trivedi, High-T_c superconductors: A variational theory of the superconducting state, Phys. Rev. B **70**, 054504 (2004).

[35] J. Spałek, M. Zegrodnik, and J. Kaczmarczyk, Universal properties of high-temperature superconductors from real-space pairing: t-J-U model and its quantitative comparison with experiment, Phys. Rev. B **95**, 024506 (2017).

[36] R. Schumann, Thermodynamics of a 4-site Hubbard model by analytical diagonalization, Ann. Phys. (Leipzig) **11**, 49 (2002).

[37] P. A. Lee, N. Nagaosa, and X. G. Wen, Doping a Mott insulator: Physics of high-temperature superconductivity, Rev. Mod. Phys. **78**, 17 (2006).

[38] P. A. Lee, From high temperature superconductivity to quantum spin liquid: Progress in strong correlation physics, Rep. Prog. Phys. **71**, 012501 (2008).

[39] J. Hubbard, Generalized Wigner lattices in one dimension and some applications to tetracyanoquinodimethane (TCNQ) salts, Phys. Rev. B **17**, 494 (1978).

[40] D. Baeriswyl D. Eichenberger, and M. Menteshashvili, Variational ground states of the two-dimensional Hubbard model, New J. Phys. **11**, 075010 (2009).

[41] H. Yokoyama, M. Ogata, and Y. Tanaka, Mott transitions and d-wave superconductivity in half-filled-band Hubbard model on square lattice with geometric frustration, J. Phys. Soc. Jpn. **75**, 114706 (2006).

[42] F. Mezzacapo, A. Angelone, and G. Pupillo, Two holes in a two-dimensional quantum antiferromagnet: A variational study based on entangled-plaquette states, Phys. Rev. B **94**, 155120 (2016).

[43] C. Regal, Bringing order to neutral atom arrays, Science **354**, 972 (2016).

[44] D. Barredo, S. de Léséleuc, V. Lienhard, T. Lahaye, and A. Browaeys, An atom-by-atom assembler of defect-free arbitrary two-dimensional atomic arrays, Science **354**, 1021 (2016).

[45] M. Endres, H. Bernien, A. Keesling, H. Levine, E. R. Anschuetz, A. Krajenbrink, C. Senko, V. Vuletic, M. Greiner, and M. D. Lukin Atom-by-atom assembly of defect-free one-dimensional cold atom arrays, Science **354**, 1024 (2016).

[46] R. B. Lehoucq, D. C. Sorensen, and C. Yang, *ARPACK Users' Guide: Solution of Large-Scale Eigenvalue Problems with Implicitly Restarted Arnoldi Methods* (SIAM, Philadelphia, 1998).

[47] Y. Li, Confined quantum fermionic systems, Ph.D. thesis, Georgia Institute of Technology, 2009.

[48] R. Pauncz, *Spin Eigenfunctions, Construction and Use* (Plenum, New York, 1979).